INTERNATIONAL JOURNAL FOR NUMERICAL METHODS IN FLUIDS
Int. J. Numer. Meth. Fluids 2004; **46**:1025–1047

Meshfree weak–strong (MWS) form method and its application to incompressible flow problems

G. R. Liu*,†,‡, Y. L. Wu and H. Ding

Department of Mechanical Engineering, Centre for Advanced Computations in Engineering Science (ACES), and National University of Singapore, 10 Kent Ridge Crescent, Singapore 119260, Singapore

SUMMARY

A meshfree weak–strong (MWS) form method has been proposed by the authors' group for linear solid mechanics problems based on a combined weak and strong form of governing equations. This paper formulates the MWS method for the incompressible Navier–Stokes equations that is non-linear in nature. In this method, the meshfree collocation method based on strong form equations is applied to the interior nodes and the nodes on the essential boundaries; the local Petrov–Galerkin weak form is applied only to the nodes on the natural boundaries of the problem domain. The MWS method is then applied to simulate the steady problem of natural convection in an enclosed domain and the unsteady problem of viscous flow around a circular cylinder using both regular and irregular nodal distributions. The simulation results are validated by comparing with those of other numerical methods as well as experimental data. It is demonstrated that the MWS method has very good efficiency and accuracy for fluid flow problems. It works perfectly well for irregular nodes using only local quadrature cells for nodes on the natural boundary, which can be generated without any difficulty.

KEY WORDS: meshfree method; MWS; moving least squares; radial basis functions approximation; vorticity-stream function; incompressible flow; natural convection; flow around a circular cylinder

1. INTRODUCTION

In recent years, meshfree methods, which are numerical approaches to avoid problems related to the creation and the use of meshes in the traditional numerical methods (such as finite difference method and finite element method), have been developed to solve engineering problems (see, e.g. Reference [1]). In general, meshfree methods developed so far fall into three categories. The first category is the meshfree methods based on the strong form equations, such as the smooth particle hydrodynamics (SPH) method [2], the general finite difference method

---

[*] Correspondence to: G. R. Liu, Department of Mechanical Engineering, Centre for Advanced Computations in Engineering Science (ACES), National University of Singapore, 10 Kent Ridge Crescent, Singapore 119260, Singapore.
[†] E-mail: mpeliugr@nus.edu.sg
[‡] SMA Fellow, Singapore-MIT Alliance (SMA).

Received 20 September 2003
Revised 19 June 2004

(GFDM) [3], the finite point method (FPM) [4], and other meshfree collocation methods. The second category is the meshfree methods based on the weak form equations, such as the element free Galerkin (EFG) method [5], the meshless local Petrov–Galerkin (MLPG) method [6–9], the local radial point interpolation method (LRPIM) [10, 11], and the boundary-type meshfree methods [12–14]. The third category is the meshfree method based on a combined formulation using both weak and strong forms, such as the meshfree weak-strong (MWS) form method [15, 16].

The attractive advantage of the meshfree collocation methods is that they are simple to implement and computationally efficient since no numerical integration is involved. However, for meshfree collocation methods based on strong form equations, there exists the difficulty to impose the Neumann (natural) boundary condition. It is known that the straightforward satisfaction of the Neumann boundary condition in strong form sense leads to unstable results [4]. In their FPM method, Oñate *et al.* [4] found that it is necessary to apply the so-called 'residual stabilization' technique to the Neumann boundary condition to ensure a correct solution. This treatment of boundary conditions is quite complex, especially for the natural boundary conditions of higher order derivatives. Cheng and Liu [17, 18] and Xu and Liu [19] have used regular nodes for Neumann boundary conditions in their meshfree procedures based on strong form. Shu *et al.* [20] used several layers orthogonal grid near and on the boundary for the Neumann boundary conditions. However, this treatment makes their local RBF-DQ method not 'truly' meshfree method, because they still need a regular grid, even though it is only generated near the boundary.

On the contrary, the weak form method treats the Neumann boundary condition naturally and easily. In addition, the accuracy achieved by meshfree methods based on the weak form equations are generally much better than those based on strong form equations. However, the efficiency is a big problem for the weak form methods because of the need for weak form integration. This is especially true for the problems of fluid flows because iterations have to be introduced due to the inherent non-linear property of N–S equations [21].

The MWS method proposed recently by Liu and Gu [15, 16] was for linear solid mechanics problems based on both collocation and local Petrov–Galerkin formulation. The MWS method uses both weak and strong form formulation to obtain stable solutions using minimum cell for background integration. In this paper, the MWS method is formulated for fluid dynamics problems that are non-linear in nature. In the present MWS method, the strong form of meshfree collocation method is applied to the internal nodes and the nodes on the essential boundaries, while the local Petrov–Galerkin weak form is applied to the nodes on the natural boundaries. This is can be done because both collocation method and local weak form method construct the discrete system equations node-by-node. The advantages of this MWS method are:

(1) The Neumann boundary condition can be imposed straightforwardly and accurately with arbitrary nodal distributions.
(2) Very stable and accurate solution can be obtained with high efficiency.

It should be emphasized that the present MWS method can be formulated using any schemes of meshfree interpolations, such as the moving least squares (MLS) and point interpolation with radial basis functions. All these interpolation schemes can be used for function approximation in the strong form equations or as the trial functions for weak form equations. In this paper, both the MLS approximation and the radial point interpolation (RPI) are used for field function approximation based on a set of irregularly scattered nodes. The MWS method based on the MLS scheme is termed as 'MWS-MLS' method, while the one based on the RPI scheme is termed as the 'MWS-RPI' method for the convenience of description in this paper.

The MWS method formulated in this paper is then applied to simulate steady and unsteady incompressible flows, which are governed by the Navier–Stokes equations in term of vorticity-stream function formulation. To demonstrate the robustness of the MWS method to irregular geometries of the problem domain and random nodal distributions, a number of examples are presented.

2. INTERPOLATION SCHEME FOR IRREGULARLY SCATTERED NODES

The interpolation scheme for irregularly scattered nodes plays a very important role in a meshfree method. Currently, there are a number of such scheme have been proposed. In this paper, two well-known meshfree interpolation schemes, the MLS and the RPI, are used for the field function approximations. The following briefs these two schemes, whose details can be found in the monograph by Liu [1].

2.1. MLS

The MLS scheme provides smooth approximations of function values using a set of randomly distributed nodes, and widely used for surface fitting [22]. Therefore, the MLS scheme is most often used as a local approximation to represent the trial functions in many meshfree methods, such as the EFG and the MLPG method. Given a column vector of nodal values of a field function $\mathbf{U}_s = \{u_1, u_2, \ldots, u_n\}^{\mathrm{T}}$, where n is the number of nodes used in the support domain Ω_s for an arbitrary point of interest at $\mathbf{x}$ located in the problem domain, the MLS approximation of the function value $u(\mathbf{x})$ at the point $\mathbf{x}$ is given by

$$u^h(\mathbf{x}) = \mathbf{\Phi}(\mathbf{x})\mathbf{U}_s \tag{1}$$

where the shape functions $\mathbf{\Phi}(\mathbf{x})$ is given by

$$\mathbf{\Phi}^{\mathrm{T}}(\mathbf{x}) = \mathbf{p}(\mathbf{x})\mathbf{A}^{-1}\mathbf{B} \tag{2}$$

in which $\mathbf{p}$ is a vector of polynomial base functions. A complete polynomial basis of order k is given by

$$\mathbf{p}^{\mathrm{T}}(\mathbf{x}) = \mathbf{p}^{\mathrm{T}}(x, y) = \{1, x, y, xy, x^2, y^2, \ldots, x^k, y^k\} \tag{3}$$

In Equation (2), $\mathbf{A} = \sum_i \mathbf{p}^{\mathrm{T}}(\mathbf{x}_i) w_i \mathbf{p}(\mathbf{x}_i), \mathbf{B} = [\ldots, w_i \mathbf{p}^{\mathrm{T}}(\mathbf{x}_i), \ldots]$, where w_i is a weight function that can have many forms (see, e.g. Reference [1]). The following well-known fourth order spline weight function is used in this work:

$$w_i(\mathbf{x}) = \begin{cases} 1 - 6\left(\dfrac{d_i}{r_w}\right)^2 + 8\left(\dfrac{d_i}{r_w}\right)^3 - 3\left(\dfrac{d_i}{r_w}\right)^4, & 0 \leqslant d_i \leqslant r_w \\ 0, & d_i \geqslant r_w \end{cases} \tag{4}$$

where $d_i = |\mathbf{x} - \mathbf{x}_i|$ is the distance from node $\mathbf{x}_i$ to point $\mathbf{x}$, r_w is the radius of the weight function domain Ω_W. In the MLS scheme, the support domain is naturally taken as the weight function domain, and r_w equals to the radius of the support domain r_s.

The non-singularity of $\mathbf{A}$ requires

$$n > m \tag{5}$$

where m is the number of terms of the polynomial basis $p(\mathbf{x})$, and n is the number of nodes in the support domain for constructing the shape function. In this paper, the polynomial $\mathbf{p}(\mathbf{x})$ of complete second order is adopted, i.e.

$$\mathbf{p}^{\mathrm{T}}(\mathbf{x}) = \mathbf{p}^{\mathrm{T}}(x, y) = \{1, x, y, xy, x^2, y^2\}, \quad m = 6 \tag{6}$$

To make sure the number of nodes n (which can be determined by counting all the nodes in the support domain) is larger than m, the support domain should be sufficiently large. Following the notation in the book by Liu [1], r_s can be written as

$$r_s = \alpha_s d_c \tag{7}$$

where α_s is the dimensionless size of support domain, d_c is a characteristic length that is taken as the average nodal spacing in the support domain of node i. It is clear that the dimensionless size of support domain α_s in Equation (7) must be large enough to produce a non-singular matrix $\mathbf{A}$. However, if α_s is too large, it can affect the accuracy of the results, the stability of the iteration, and the efficiency of the computation. Through a number of numerical tests, we found that $\alpha_s = 2.5$–3.5 can give very good results for our problems.

To determine the spatial derivatives of the field variables, it is necessary to obtain the derivatives of the MLS shape functions. The standard procedure of determining the partial derivatives of the shape function is as follows [1]:

(1) Equation (2) can be rewritten as:

$$\mathbf{\Phi}(\mathbf{x}) = \boldsymbol{\gamma}^{\mathrm{T}}(\mathbf{x})\mathbf{B}(\mathbf{x}) \tag{8}$$

where $\boldsymbol{\gamma}(\mathbf{x})$ can be determined by

$$\mathbf{A}(\mathbf{x})\boldsymbol{\gamma}(\mathbf{x}) = \mathbf{p}(\mathbf{x}) \tag{9}$$

(2) The partial derivatives of $\boldsymbol{\gamma}(\mathbf{x})$ can be obtained as follows:

$$\mathbf{A}\boldsymbol{\gamma}_{,i} = \mathbf{p}_{,i} - \mathbf{A}_{,i}\boldsymbol{\gamma} \tag{10}$$

$$\mathbf{A}\boldsymbol{\gamma}_{,ij} = \mathbf{p}_{,ij} - (\mathbf{A}_{,i}\boldsymbol{\gamma}_{,j} + \mathbf{A}_{,j}\boldsymbol{\gamma}_{,i} + \mathbf{A}_{,ij}\boldsymbol{\gamma}) \tag{11}$$

where i and j denote spatial co-ordinates x and y, respectively. A comma designates a partial differentiation with respect to the indicated spatial co-ordinate.

(3) The partial derivatives of the shape function can then be obtained as follows:

$$\mathbf{\Phi}_{,i} = \boldsymbol{\gamma}_{,i}\mathbf{B} + \boldsymbol{\gamma}\mathbf{B}_{,i} \tag{12}$$

$$\mathbf{\Phi}_{,ij} = \boldsymbol{\gamma}_{,ij}\mathbf{B} + \boldsymbol{\gamma}_{,i}\mathbf{B}_{,j} + \boldsymbol{\gamma}_{,j}\mathbf{B}_{,i} + \boldsymbol{\gamma}\mathbf{B}_{,ij} \tag{13}$$

2.2. *RPI scheme*

Radial basis functions (RBF) is also widely used in surface fitting [23] as well as solving strong form partial differential equations (PDEs) [24]. Suppose there are n nodes, $\mathbf{x}_1,\ldots,\mathbf{x}_n$, in the support domain of point $\mathbf{x}$, and the vector of these nodal values of a field function is denoted as $\mathbf{U}_s=\{u_1,u_2,\ldots,u_n\}^{\mathrm{T}}$. The approximation of u by the RPI scheme can be written in the form of

$$u^h(\mathbf{x},\mathbf{x}_Q)=\sum_{i=1}^{n} R_i(\mathbf{x})a_i(\mathbf{x}_Q)=\mathbf{R}^{\mathrm{T}}(\mathbf{x})\mathbf{a}(\mathbf{x}_Q) \tag{14}$$

where R_i is a radial basis function, and $a_i(\mathbf{x}_Q)$ is the coefficient for R_i corresponding to the given point $\mathbf{x}_Q$. The coefficient vector $\mathbf{a}$ in Equation (14) is determined by

$$\mathbf{a}=\mathbf{R}_Q^{-1}\mathbf{U}_s \tag{15}$$

Substitute Equation (15) into (14) to obtain

$$u^h(\mathbf{x})=R^{\mathrm{T}}(\mathbf{x})R_Q^{-1}\mathbf{U}_s=\mathbf{\Phi}(\mathbf{x})\mathbf{U}_s \tag{16}$$

The derivatives of the shape functions can be easily obtained as

$$\begin{aligned}\frac{\partial\mathbf{\Phi}}{\partial x}&=\left[\frac{\partial R_1}{\partial x},\ \frac{\partial R_2}{\partial x},\ldots,\ \frac{\partial R_n}{\partial x}\right]R_Q^{-1}\\ \frac{\partial\mathbf{\Phi}}{\partial y}&=\left[\frac{\partial R_1}{\partial y},\ \frac{\partial R_2}{\partial y},\ldots,\ \frac{\partial R_n}{\partial y}\right]R_Q^{-1}\end{aligned} \tag{17}$$

For good performance, we choose MQ RBF as the basis function in this paper, which can be written as

$$R_i(x,y)=(r_i^2+C^2)^q=[(x-x_i)^2+(y-y_i)^2+C^2]^q \tag{18}$$

where the positive constants C, q are called shape parameters, and r_i is the distance between points at $\mathbf{x}$ and $\mathbf{x}_i$.

It is well known that the accuracy of RBF approximation depends heavily on the choice of the shape parameters. As shown in Reference [1], C is defined as

$$C=\alpha_C d_c \tag{19}$$

where, α_C is a dimensionless shape parameter, d_c is a characteristic length which is the shortest distance between the node i and neighbour nodes. Therefore, the RBF function and its derivatives can be written as:

$$R_i(x,y)=[r_i^2+(\alpha_C d_c)^2]^q \tag{20}$$

$$R_{i,x}=2q[r_i^2+(\alpha_C d_c)^2]^{q-1}(x-x_i) \tag{21}$$

$$R_{i,y}=2q[r_i^2+(\alpha_C d_c)^2]^{q-1}(y-y_i) \tag{22}$$

$$R_{i,xx}=2q[r_i^2+(\alpha_C d_c)^2]^{q-1}+4q(q-1)[r_i^2+(\alpha_C d_c)^2]^{q-2}(x-x_i)^2 \tag{23}$$

$$R_{i,yy}=2q[r_i^2+(\alpha_C d_c)^2]^{q-1}+4q(q-1)[r_i^2+(\alpha_C d_c)^2]^{q-2}(y-y_i)^2 \tag{24}$$

It is found that the choice of α_C, q and the number of nodes in the support domain n can influence the accuracy of the solution [1]. In their paper Wu and Liu [21], gave preliminary study on the effects of α_C and n when $q = 1.03$.

3. FORMULATION OF THE MWS METHOD

Collocation method has been widely used for solving PDEs [25]. As mentioned in Section 1, the MWS method uses a combined formulation of both weak and strong forms.

In the following, a two-dimensional Poisson equation is used to present the procedure of the MWS method. The Poisson equation can be written as

$$\nabla^2 u(\mathbf{x}) = f(\mathbf{x}), \quad \mathbf{x} \in \Omega \tag{25}$$

where $f(\mathbf{x})$ is a given source function, and $u(\mathbf{x})$ is the field function defined in the domain Ω is enclosed by $\Gamma = \Gamma_u \cup \Gamma_t$, with boundary conditions of

$$u_i = \bar{u}_i \quad \text{on } \Gamma_u \tag{26}$$

$$\left.\frac{\partial u}{\partial \vec{n}}\right|_i = \bar{t}_i \quad \text{on } \Gamma_t \tag{27}$$

where Γ_u denotes the essential boundary and Γ_t is the natural boundary.

3.1. Meshfree collocation method

In the meshfree collocation method, at each node in the problem domain, the derivatives in the given strong form of PDE can be approximated by a meshfree interpolation scheme. A set of discretized equations for the nodes can be obtained. Each of the equations consists of the values of field variables at the nodes in the support domain of the node of interest. For a node i at position $\mathbf{x}_i$, Equation (25) can be discretized as

$$\sum_{k=1}^{n} [\phi_i(\mathbf{x}_k)]_{xx} u_k + \sum_{k=1}^{n} [\phi_i(\mathbf{x}_k)]_{yy} u_k = f_i \tag{28}$$

where n is the number of nodes in the support domain of the node at $\mathbf{x}_i$.

If the process is repeated at a set of nodes, a set of equations for the field variable u at these nodes are formed.

3.2. Implementation of essential boundary condition

In general, the MLS approximation does not pass through the nodal data. Therefore, the essential boundary conditions cannot be imposed directly. The direct interpolation procedure is often used to enforce the essential boundary condition [12–14, 26, 27], which is adopted in this paper, i.e.

$$u_i^h(\mathbf{x}) = \sum_{k=1}^{n} \phi_i(\mathbf{x}_k) u_k = \bar{u}_i \tag{29}$$

When RPI scheme is used, because the RPI approximation passes through the nodal data, the shape function $\phi(\mathbf{x})$ obtained using Equation (16) possesses delta function property, i.e.

$$\phi_i(\mathbf{x}_k) = \delta_{ik} = \begin{cases} 1, & i = k \\ 0, & i \neq k \end{cases} \tag{30}$$

Therefore, the discrete equation for the Dirichlet (essential) boundary can be written directly in the same form of Equation (26).

3.3. Imposition of the natural boundary condition

In MWS method, the natural boundary condition is imposed using the local weak form method. Local weak form was firstly proposed by Atluri and Zhu [6] in their MLPG method, in which the equilibrium equations are satisfied at each node in a local weak sense by applying the weighted residual method over a local quadrature cell. Based on the concept of the MLPG, a so-called LRPIM has also been proposed [10] using RPI scheme. In the MWS method, the local weak form method which is used to implement the natural boundary condition, is actually the MLPG method when the MLS scheme is adopted as the interpolation scheme; or the LRPIM method if the RPI scheme is used as the meshfree interpolation scheme.

A local Petrov–Galerkin weak form of the differential equation (25) for a node at the natural boundary, say node *i*, can be written as:

$$\int_{\Omega_Q} (\nabla^2 u - f) w_i \, \mathrm{d}\Omega = 0 \tag{31}$$

where w is the test function, which has the same expression as Equation (4). Ω_Q is the quadrature domain for the node *i*, which is a regular shape cell (such as a circle in this paper) in 2-D centred at the node *i*.

Using the divergence theorem, one obtains

$$\int_{\Gamma_Q} u_{,j} n_j w_i \, \mathrm{d}\Gamma - \int_{\Omega_Q} (u_{,j} w_{i,j} + f w_i) \, \mathrm{d}\Omega = 0 \tag{32}$$

in which Γ_Q is the boundary of $\mathbf{\Omega}_Q$ and $\vec{n}$ is the outward unit normal to the boundary Γ_Q. Imposing the natural boundary condition, we have,

$$\int_{\Gamma_{Qi}} u_{,j} n_j w_i \, \mathrm{d}\Gamma + \int_{\Gamma_{Qu}} u_{,j} n_j w_i \, \mathrm{d}\Gamma + \int_{\Gamma_{Qt}} \bar{t}_i w_i \, \mathrm{d}\Gamma - \int_{\Omega_Q} (u_{,j} w_{i,j} + f w_i) \, \mathrm{d}\Omega = 0 \tag{33}$$

here Γ_{Qu} is the intersection of Γ_Q and the essential boundary Γ_u, Γ_{Qt} is a part of Γ_Q over which the natural boundary condition, $u_{,i} n_i = \bar{t}_i$, is specified, and Γ_{Qi} is the internal part of Γ_Q on which no boundary condition is specified.

Theoretically, the quadrature domain Ω_Q and the weight function domain Ω_W do not have to be the same. However, in practice we often use the same for both, so the curve integration along the interior boundary Γ_{Qi} vanishes, and Equation (33) is simplified to

$$\int_{\Omega_Q} u_{,j} w_{i,j} \, \mathrm{d}\Omega - \int_{\Gamma_{Qu}} u_{,j} n_j w_i \, \mathrm{d}\Gamma = \int_{\Gamma_{Qt}} \bar{t}_i w_i \, \mathrm{d}\Gamma - \int_{\Omega_Q} f w_i \, \mathrm{d}\Omega \tag{34}$$

Equation (34) is used to establish the discrete equations for all the nodes at natural boundary. As defined in Reference [1], r_Q can be written as

$$r_Q = \alpha_Q d_c \tag{35}$$

where α_Q is the dimensionless size of quadrature domain, and $\alpha_Q = 1.0$–2.0 is used in this study. d_c is the shortest nodal spacing between the node i and its neighbour nodes.

4. APPLICATION OF MWS METHOD TO INCOMPRESSIBLE FLOW PROBLEMS

4.1. Simulation of natural convection in enclosed domain

4.1.1. Governing equations and numerical discretization. The problem domain is given in Figure 1. The governing equations of natural convection in an enclosed domain can be written in the Cartesian co-ordinate system:

$$\frac{\partial^2\psi}{\partial x^2} + \frac{\partial^2\psi}{\partial y^2} = \omega \tag{36}$$

$$u\frac{\partial\omega}{\partial x} + v\frac{\partial\omega}{\partial y} = Pr\left(\frac{\partial^2\omega}{\partial x^2} + \frac{\partial^2\omega}{\partial y^2}\right) - Pr\,Ra\frac{\partial T}{\partial x} \tag{37}$$

$$u\frac{\partial T}{\partial x} + v\frac{\partial T}{\partial y} = \frac{\partial^2 T}{\partial x^2} + \frac{\partial^2 T}{\partial y^2} \tag{38}$$

where

$$u = \frac{\partial\psi}{\partial y}, \quad v = -\frac{\partial\psi}{\partial x} \tag{39}$$

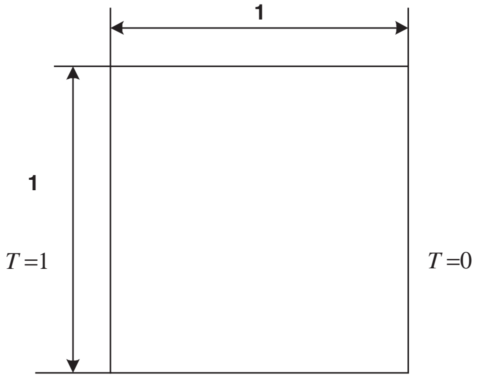

Figure 1. Schematic drawing of the problem domain.

The boundary conditions are listed below:

$$(1) \quad x=0, 0 \leqslant y \leqslant 1: \ \psi=0, \frac{\partial \psi}{\partial x}=0, T=1 \tag{40}$$

$$(2) \quad x=1, 0 \leqslant y \leqslant 1: \ \psi=0, \frac{\partial \psi}{\partial x}=0, T=0 \tag{41}$$

$$(3) \quad y=0, 0 \leqslant x \leqslant 1: \ \psi=0, \frac{\partial \psi}{\partial y}=0, \frac{\partial T}{\partial y}=0 \tag{42}$$

$$(4) \quad y=1, 0 \leqslant x \leqslant 1: \ \psi=0, \frac{\partial \psi}{\partial y}=0, \frac{\partial T}{\partial y}=0 \tag{43}$$

It is clear that there are two types of conditions: one is the Dirichlet type, the other is the Neumann type.

According to Section 3, the discretized equation can be written as:

(1) For an interior node i:

$$\sum_{k=1}^{n}(\phi_k)_{xx}\psi_k + \sum_{k=1}^{n}(\phi_k)_{yy}\psi_k = \omega_i \tag{44}$$

$$u_i \sum_{k=1}^{n}(\phi_k)_x\omega_k + v_i \sum_{k=1}^{n}(\phi_k)_y\omega_k = Pr\left(\sum_{k=1}^{n}(\phi_k)_{xx}\omega_k + \sum_{k=1}^{n}(\phi_k)_{yy}\omega_k\right) - RaPr\sum_{k=1}^{n}(\phi_k)_x T_k \tag{45}$$

$$u_i \sum_{k=1}^{n}(\phi_k)_x T_k + v_i \sum_{k=1}^{n}(\phi_k)_y T_k = \sum_{k=1}^{n}(\phi_k)_{xx} T_k + \sum_{k=1}^{n}(\phi_k)_{yy} T_k \tag{46}$$

$$u_i = \sum_{k=1}^{n}(\phi_k)_x\psi_k, \quad v_i = \sum_{k=1}^{n}(\phi_k)_y\psi_k \tag{47}$$

Note here $\phi_k \equiv \phi_i(\mathbf{x}_k)$.

(2) For a node at the natural boundary:

$$C_{ik}\psi_k - E_{ik}\psi_k = -A_{ik}\omega_k \tag{48}$$

$$B_{ik}\omega_k + Pr\, C_{ik}\omega_k - Pr\, E_{ik}\omega_k = -Pr\, Ra\, D_{ik} T_k \tag{49}$$

$$B_{ik} T_k + C_{ik} T_k - E_{ik} T_k = 0 \tag{50}$$

where

$$A_{ik} = \iint_{\Omega_Q} \phi_k w_i \, \mathrm{d}\Omega \tag{51}$$

$$B_{ik} = \iint_{\Omega_Q} \left[u \cdot \frac{\partial \phi_k}{\partial x} + v \cdot \frac{\partial \phi_k}{\partial y} \right] \cdot w_i \, \mathrm{d}\Omega \tag{52}$$

$$C_{ik} = \iint_{\Omega_Q} \left(\frac{\partial \phi_k}{\partial x} \frac{\partial w_i}{\partial x} + \frac{\partial \phi_k}{\partial y} \frac{\partial w_i}{\partial y} \right) \mathrm{d}\Omega \tag{53}$$

$$D_{ik} = \iint_{\Omega_Q} \frac{\partial \phi_k}{\partial x} w_i \, \mathrm{d}\Omega \tag{54}$$

$$E_{ik} = \int_{\Gamma_{Qu}} \frac{\partial \phi_k}{\partial \vec{n}} w_i \, \mathrm{d}\Gamma \tag{55}$$

where $w_i(\mathbf{x})$ is the nodal test function, as shown in Equation (4). The single integration E_{ik} along Γ_{Qu} is implemented appropriately according to different essential boundary conditions for ω, ψ and T. The double integration for A_{ik}, B_{ik}, C_{ik}, and D_{ik} can be evaluated by the Gauss quadrature scheme using the transformation strategy according to Wu and Liu [21]. Note that all these integrations can be carried out on the local regular shape cell centred at the nodes only on the natural boundary. Therefore, the numerical integration can always be implemented without any difficulty.

(3) For a node on the essential boundary:
The essential boundary conditions for ψ and T are

$$\begin{aligned} &\psi_i = 0, \text{ when node } i \text{ is on the whole wall boundary} \\ &T_i = 1, \text{ when node } i \text{ is on the hot wall} \\ &T_i = 0, \text{ when node } i \text{ is on the cool wall} \end{aligned} \tag{56}$$

The essential boundary condition can be directly imposed using Equation (29) for MWS-MLS or using Equation (30) for MWS-RPI.

(4) The boundary condition for vorticity ω:
There is no explicit boundary condition for vorticity. However, it is found from Equation (36) that the implementation of vorticity condition is equivalent to approximate the second order derivatives of the stream function at the boundary. Therefore, the Dirichlet boundary condition for vorticity ω can be interpreted as the Neumann boundary condition for the stream function ψ. Thus, the boundary condition for vorticity can be derived by taking the local weak form of Equation (36) on the wall boundary, as shown in Equation (48), i.e.:

$$-A_{ik}\omega_k = (C_{ik}\psi_k - E_{ik}\psi_k) \tag{57}$$

4.1.2. Numerical results and discussion. The resultant algebraic equations (44)–(50) are a set of non-linear equations. Therefore, an iterative loop is needed to solve this set of equations. When the L_∞ norm of residuals for the equations for ψ, ω and T in Equations (44)–(46) as well as Equations (48)–(50) are less than 10^{-3}, the calculation is considered to be converged.

Different nodal distributions are used for the square cavity problem to validate the present MWS method, as shown in Figure 2. For the case of the cavity flow, in order to compare the accuracy of the results obtained using the present method and that of other methods, such as MLPG method, LRPIM method, and the finite difference (FD) method, the following

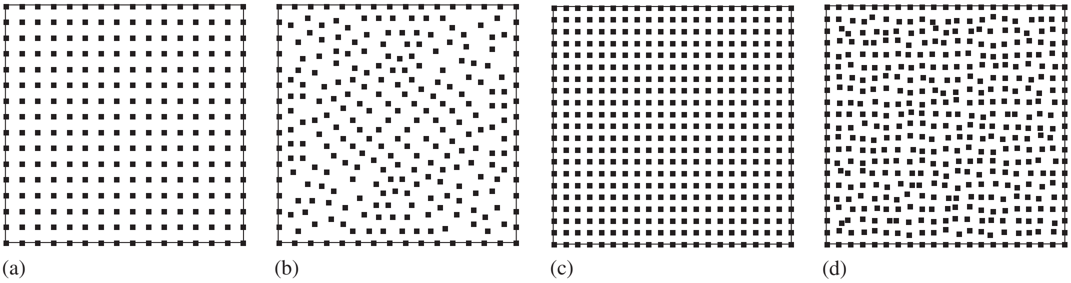

Figure 2. Different nodal distributions for the square cavity problem: (a) 256 regular nodes; (b) 268 scattered nodes; (c) 441 regular nodes; and (d) 441 scattered nodes.

quantities are calculated:

$|\psi_{\max}|$, maximum absolute value of the stream function

$u_{\max}$, maximum horizontal velocity on the vertical mid-plane of the cavity

$v_{\max}$, maximum vertical velocity on the horizontal mid-plane of the cavity

$Nu_{\max}$, maximum value of the local Nusselt number on the boundary at $x = 0$

$Nu_{\min}$, minimum value of the local Nusselt number on the boundary at $x = 0$

Nu is the local *Nusselt* number which is defined as

$$Nu|_{x=0} = -\left.\frac{\partial T}{\partial x}\right|_{x=0} \tag{58}$$

The 'energy norm' of error E_r, which is defined as mean square of the relative error of the above five quantities, is used as an error indicator for comparison. Since there is no analytical solution for the problem, the benchmark numerical solution of Davis [28] is adopted as the 'true' solution to the cavity problem.

The main feature of the meshfree methods is that they obtain numerical solution using randomly distributed nodes. In order to determine the maximum and minimum variable values in the whole problem domain, after the converged solution on field nodes is obtained, the functional values on a fine uniform mesh of 101 × 101 are calculated. This can be done by the corresponding interpolation procedure which was used in the discretization process for different methods. It is noted that the uniform mesh of 101 × 101 is independent of the implementation of different methods, as it is only used for the post-visualization. In the following, all the results shown in the tables and figures are based on the functional values on the post-visualization mesh.

First, we compared the rates of convergence and corresponding running time required for the present MWS methods, MLPG method, LRPIM method and FD method in the case of $Ra = 10^3$, using the same uniform nodal distribution. It should be noted that, for the purpose of comparison, all the parameters in the meshfree interpolation schemes are kept the same for

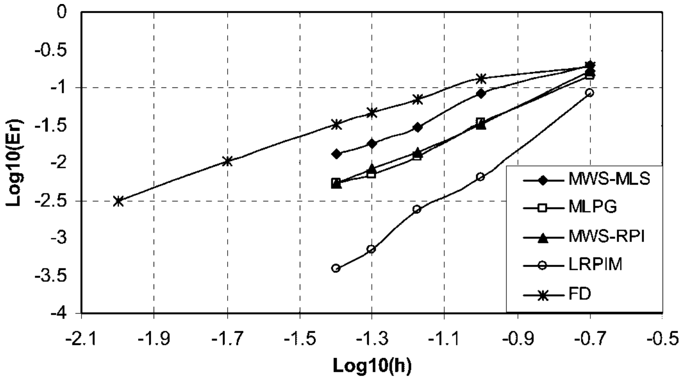

Figure 3. Comparison of convergence rates for different methods.

the MWS methods and their full weak form methods. For example, the dimensionless size of support domain α_s for MLS scheme is taken as 3.0 for both the MWS-MLS and MLPG method. The dimensionless shape parameter α_C, shape parameter q, and the number of nodes in the support domain n in RPI scheme are taken as $\alpha_C = 8$, $q = 1.03$, $n = 30$, respectively, for both the MWS-RPI and the LRPIM. Figure 3 shows the results, where h is the nodal spacing. It is very clear that MWS method is much more accurate than FD when h is decreased. However, the MWS method is less accurate than the meshfree method where the local weak form is used for all the nodes. In other words, the MWS-MLS method is less accurate than the MLPG method, and the MWS-RPI method is less accurate than the LRPIM method. The LRPIM method is the most accurate method. In general, the MLS-based meshfree method is less accurate than the RPI-based method.

However, the main drawback of the RPI-based method is that the accuracy depends on the proper choice of the shape parameters. Up to date, there is no general mathematical theory has been developed for determining the optimal values of the shape parameters in radial basis function approximation. Wu and Liu [21] found that although the accuracy of approximation is improved when α_C and n increase, the computation may run high risk to be crippled when they are too large, especially when the approximated function is very complex. Therefore, for present MWS-RPI method in the case of $Ra = 10^3, 10^4$, α_C can be chosen from 6 to 9 for $n = 20$–30, and very accurate results can be obtained. For the case of $Ra = 10^5$, to achieve good accuracy, α_C should be around 1, and n should not be larger than 12.

Figure 4 shows the running time against the number of field nodes in the problem domain N for the MWS methods and its full weak-form counterparts. The running time is obtained by testing the methods on a Compaq Alpha-server supercomputer. Note that the number of field nodes N is corresponding to the different nodal spacing h in Figure 3. From the simulation, it is found that both the MWS-MLS method and the MLPG method cannot get converged results using the iterative scheme to solve the algebraic equations. Therefore, the resultant algebraic equations are solved by an amended Gaussian elimination procedure at each iteration step. It is found from Figure 4(a) that the running time of the MWS-MLS is much less than that of the MLPG method. This is because in the MLPG method, a lot of time is consumed in constructing the shape function for the Gaussian points inside the quadrature domain for each

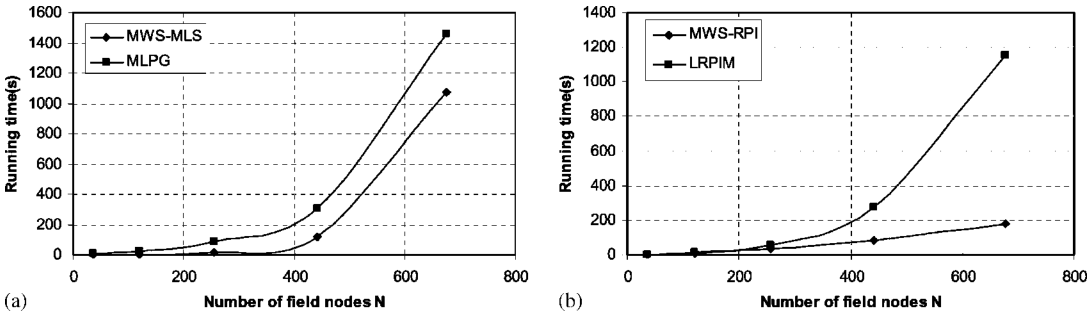

Figure 4. Comparison of running time between the MWS and their full weak-form counterparts for different field nodes: (a) MWS-MLS vs MLPG; and (b) MWS-RPI vs LRPIM.

Table I. Comparison of numerical results for natural convection in the square cavity problem for $Ra = 10^3$.

Method	Nodal distribution	$\lvert\psi_{\max}\rvert$	$u_{\max}$	$v_{\max}$	$Nu_{\max}$	$Nu_{\min}$
MWS-MLS	256 Regular nodes	1.117	3.546	3.609	1.477	0.706
	268 Scattered nodes	1.140	3.696	3.594	1.498	0.718
MWS-RPI	256 Regular nodes	1.196	3.681	3.734	1.528	0.684
	268 Scattered nodes	1.192	3.688	3.731	1.525	0.686
	Reference [28]	1.174	3.649	3.697	1.505	0.692

field node and numerical integration. In the MWS-MLS, however, the strong form equation is used for all the interior nodes. Therefore, only the shape functions for the field nodes are computed. These shape functions can be determined firstly and stored throughout the entire iteration process, which reduces the computational cost greatly. However, if the number of nodes is quite large, the direct solver adopted by both the MWS-MLS and MLPG method becomes very expensive.

Similarly, the MWS-RPI spends much less time on calculating the shape function for Gaussian points and numerical integration than the LRPIM method. More importantly, it is found that the point iterative scheme, such as SOR scheme can be adopted in the MWS-RPI method to solve the algebraic equations systems. Therefore, the computational complexity for the MWS-RPI is about $O(N)$. On the other hand, although the LRPIM method can achieve high accuracy using less nodes, the weak form equation over every field node makes the traditional stationary iterative scheme (such as Gauss–Seidel, SOR scheme) not to converge. Therefore, the more expensive direct solver has to be used to solve the algebraic equations systems, whose computational complexity is about $O(N^3)$. Figure 4(b) confirms this conclusion. Therefore, the MWS-RPI is much more suitable for solving large scale problem.

Tables I–III list the numerical results for different sets of nodes for cases of Rayleigh numbers of $10^3, 10^4, 10^5$, respectively. It can be observed that for all the sets of nodes, the results of the MWS method agree very well with the benchmark solution given by Davis [28]. The streamlines and isotherms for $Ra = 10^3, 10^4, 10^5$ are shown in Figures 5–7.

Table II. Comparison of numerical results for natural convection in the square cavity problem for $Ra = 10^4$.

Method	Nodal distribution	$\lvert\psi_{\max}\rvert$	$u_{\max}$	$v_{\max}$	$Nu_{\max}$	$Nu_{\min}$
MWS-MLS	256 Regular nodes	4.809	15.752	18.698	3.609	0.581
	268 Scattered nodes	4.963	16.689	19.427	3.746	0.543
MWS-RPI	256 Regular nodes	5.169	16.373	20.017	3.756	0.577
	268 Scattered nodes	5.174	16.447	20.071	3.740	0.580
	Reference [28]	5.071	16.178	19.617	3.528	0.586

Table III. Comparison of numerical results for natural convection in the square cavity problem for $Ra = 10^5$.

Method	Nodal distribution	$\lvert\psi_{\max}\rvert$	$u_{\max}$	$v_{\max}$	$Nu_{\max}$	$Nu_{\min}$
MWS-MLS	441 Regular nodes	9.463	36.787	61.431	8.772	0.713
	441 Irregular nodes	10.098	36.689	70.093	10.597	0.743
MWS-RPI	441 Regular nodes	9.772	35.209	66.044	10.070	0.699
	441 Irregular nodes	9.918	37.863	64.964	8.507	0.579
	Reference [28]	9.612	34.730	68.590	7.717	0.729

4.2. Simulation of the flow around a cylinder

The incompressible, viscous flow around a circular cylinder is a classical problem in fluid mechanics. Despite the simplicity of the cylinder's geometry, the flow is in fact very complex. Because of its relevance to engineering problems and importance to the fundamental understanding of fluid flow, numerous theoretical, numerical and experimental investigations of flow past a circular cylinder had been frequently reported in the past century. It serves as a very good sample problem for validating a new numerical method for solving unsteady two-dimensional Navier–Stokes equations. In this paper, the MWS method is used to solve this problem.

4.2.1. Governing equation and boundary condition. The problem addressed in this paper is simulation of an incompressible, viscous fluid flow at a constant velocity U_∞ past a stationary cylinder of radius a, as shown Figure 8.

The dimensionless two-dimensional Navier–Stokes equations in the vorticity-stream function form can be written as

$$\begin{gathered}\frac{\partial^2\psi}{\partial x^2}+\frac{\partial^2\psi}{\partial y^2}=\omega\\ \frac{\partial\omega}{\partial t}+u\frac{\partial\omega}{\partial x}+v\frac{\partial\omega}{\partial y}=\frac{1}{Re}\left(\frac{\partial^2\omega}{\partial x^2}+\frac{\partial^2\omega}{\partial y^2}\right)\end{gathered}\tag{59}$$

where Re is Reynolds number defined as $Re = U_\infty D/v$, D is the cylinder diameter, and v is the kinematic viscosity.

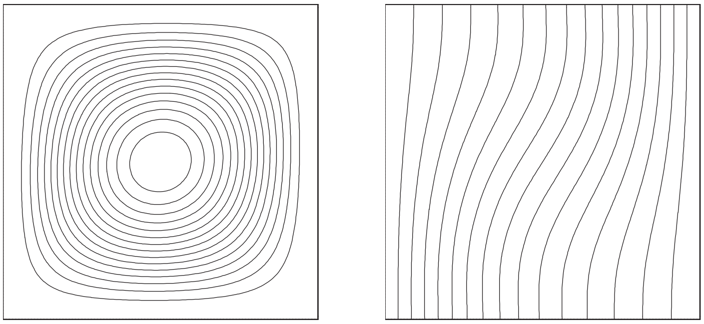

Figure 5. Streamlines and isotherms for the cavity flow ($Ra = 10^3$) obtained by the MWS-MLS method with 268 irregular nodes.

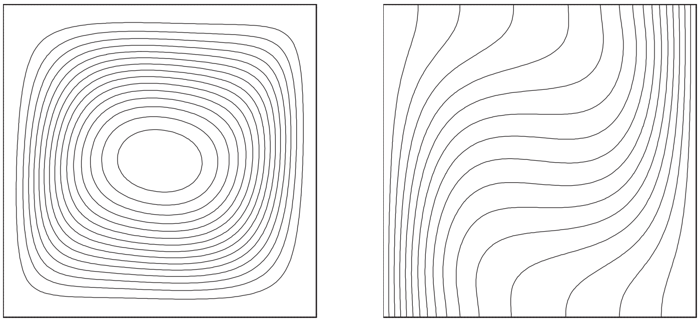

Figure 6. Streamlines and isotherms for cavity flow ($Ra = 10^4$) obtained by the MWS-RPI method with 268 irregular nodes.

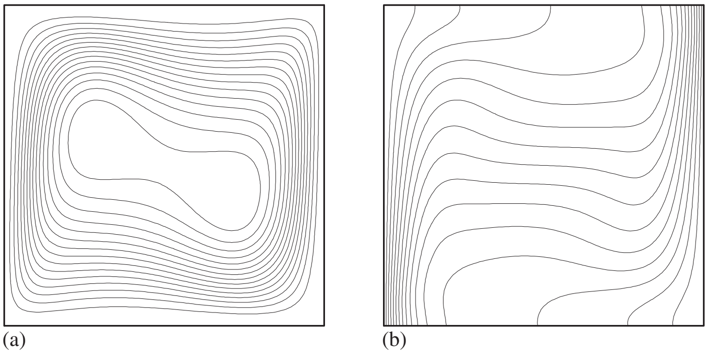

Figure 7. Streamlines and isotherms for the cavity flow ($Ra = 10^5$) obtained by MWS-RPI method with 441 irregular nodes: (a) Streamlines; and (b) isotherms.

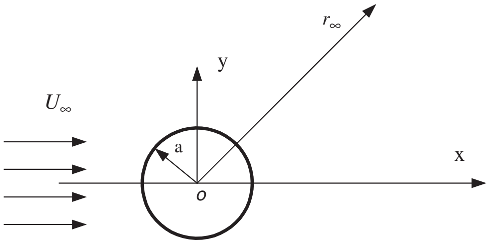

Figure 8. Schematic drawing of flow configuration.

The boundary conditions of the problem are:

(i) free stream velocity U at the in-flow boundary

$$\begin{cases} \psi = U_\infty \, y \\ \omega = 0 \end{cases} \tag{60}$$

(ii) no slip on the surface of the cylinder

$$\begin{cases} \omega = \dfrac{\partial^2 \psi}{\partial n^2} \\ \psi = 0 \end{cases} \tag{61}$$

(iii) uniform flow at infinity except downstream boundary

$$\begin{cases} \omega = 0 \\ \psi = \psi|_{\text{uniform flow}} \end{cases} \tag{62}$$

(iv) Zero-gradient condition at infinity downstream

$$\begin{cases} \dfrac{\partial \omega}{\partial x} = 0 \\ \dfrac{\partial \psi}{\partial x} = 0 \end{cases} \tag{63}$$

The initial condition for this problem is taken as an unsymmetrical initial flow field, i.e.

$$\psi|_{t=0} = \sqrt{x^2 + y^2} \tag{64}$$

which serves as an artificial initiator for the numerical simulation.

Using the same notation as in Section 4.1.1, the discretized form of strong form equations at interior nodes are:

$$\begin{gathered} \sum_{k=1}^{n} (\phi_k)_{xx} \psi_k + \sum_{k=1}^{n} (\phi_k)_{yy} \psi_k = \omega_i \\ \frac{\mathrm{d}\omega_i}{\mathrm{d}t} + u_i \sum_{k=1}^{n} (\phi_k)_x \omega_k + v_i \sum_{k=1}^{n} (\phi_k)_y \omega_k = \frac{1}{Re} \left(\sum_{k=1}^{n} (\phi_k)_{xx} \omega_k + \sum_{k=1}^{n} (\phi_k)_{yy} \omega_k \right) \end{gathered} \tag{65}$$

and the discretized equations in local weak form sense for the nodes on natural boundary in matrix form are:

$$\begin{aligned} &C_{ik}\psi_k - E_{ik}\psi_k = -A_{ik}\omega_k \\ &\frac{\mathrm{d}\omega_i}{\mathrm{d}t} + B_{ik}\omega_k + \frac{1}{Re}C_{ik}\omega_k - \frac{1}{Re}E_{ik}\omega_k = 0 \end{aligned} \tag{66}$$

where $A_{ik}, B_{ik}, C_{ik}, E_{ik}$ are defined in Equations (51)–(55). As discussed in Section 4.1.1, the boundary condition for vorticity can be discretized as Equation (57).

It is found that for the unsteady problem, there is a time derivative in Equations (65) and (66). In the present model, the time derivative is approximated using an explicit three-step formulation based on a Taylor series expansion in time [29]. From Taylor's series, a function f in time can be written as

$$f(t+\Delta t) = f(t) + \Delta t\frac{\partial f(t)}{\partial t} + \frac{\Delta t^2}{2}\frac{\partial^2 f(t)}{\partial t^2} + \frac{\Delta t^3}{6}\frac{\partial^3 f(t)}{\partial t^3} + O(\Delta t^4) \tag{67}$$

where Δt is the time interval. Approximating Equation (67) up to third-order accuracy, the three-step formulation can be written as:

$$f\left(t+\frac{\Delta t}{3}\right) = f(t) + \frac{\Delta t}{3}\frac{\partial f(t)}{\partial t} \tag{68}$$

$$f\left(t+\frac{\Delta t}{2}\right) = f(t) + \frac{\Delta t}{2}\frac{\partial f(t+\Delta t/3)}{\partial t} \tag{69}$$

$$f(t+\Delta t) = f(t) + \Delta t\frac{\partial f(t+\Delta t/2)}{\partial t} \tag{70}$$

4.2.2. Computational procedure. To solve the resultant algebraic equations, a time-matching iterative scheme is used. The computational procedure adopted here includes the following steps:

(1) assume at time $t=0$, the unsymmetrical initial flow field is given as

$$\begin{cases} \psi|_{t=0} = \sqrt{x^2+y^2} \\ \omega|_{t=0} = 0 \end{cases} \tag{71}$$

(2) calculate the unknown field values of velocities u and v via Equation (47),
(3) solve the vorticity equation using three-step time marching scheme,
(4) solve the stream-function equation by SOR scheme until the L_∞ norm of residuals for the equations for ψ is less than 10^{-2}, because the accuracy of the stream-function is very important for the stable simulation,
(5) the procedure is repeated until the prescribed time-step is reached.

4.2.3. Results and discussion. Simulations of small and moderate Reynolds number flow ($Re=20$ and 100, respectively) are carried out by using the MWS method. The computational domain is shown in Figure 9, where a is the radius of the cylinder.

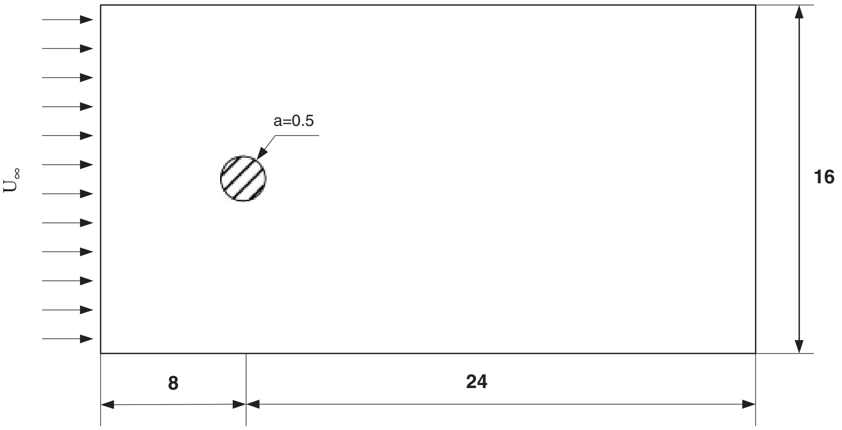

Figure 9. Problem domain for the simulation of the flow around a circular cylinder.

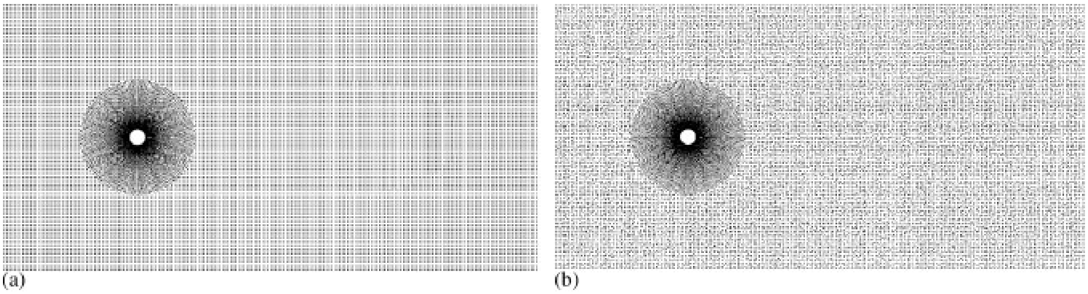

Figure 10. Two types of nodal distribution for the numerical simulation using the MWS-RPI method: (a) Type I (23 191 nodes); and (b) Type II (23 177 nodes).

In this paper, two different types of nodal distributions are adopted to validate the MWS method, as shown in Figure 10. In these two distributions, the nodes within the area $r=\sqrt{x^2+y^2}\leqslant 3.5$ are generated by MFree2D© (see, Reference [1]). The rest region is distributed by regular nodes in Type I (Figure 10(a)) and by randomly scattered nodes in Type II (Figure 10(b)). It is found that both Type I and Type II contain large number of field nodes. Therefore, in this paper, only the MWS-RPI method is used to simulate this problem due to its good efficiency for large-scale problem. The dimensionless shape parameter α_C, shape parameter q, and the number of nodes in the support domain n in present RPI scheme are taken as $\alpha_C=4$, $q=1.03$, $n=20$, respectively.

It is found that for $Re=20$, the unsymmetrical initial flow field evolves to be symmetrical and flow appear to be laminar steady flow; for $Re=100$, the flow field eventually settle into a periodic oscillatory pattern. This confirms the other experimental and numerical results. It is generally agreed that in two dimensions the vortex shedding begins at a critical Reynolds number around 49. For the Reynolds numbers less than the critical value ($Re_{\text{critical}}=49$), the introduced perturbation is gradually dissipated by viscosity. Above this critical Reynolds

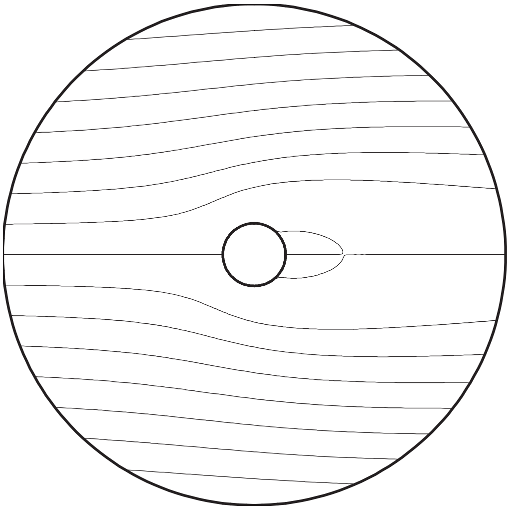

Figure 11. Streamlines at the final steady state for $Re = 20$.

Table IV. Comparison of geometrical and dynamical parameters with previous studies.

	L/a	θ_s	C_D
Reference [30]	1.88	43.7	2.045
Reference [31]	1.786	43.37	2.053
Reference [32]	1.82	—	2.000
Reference [33]	1.842	42.96	2.152
Present (Type I)	1.86	43.21	2.076
Present (Type II)	1.84	44.74	2.103

number, the introduced perturbation will trigger the vortex shedding process to form a Von Karman vortex street.

Figure 11 shows the streamlines for $Re = 20$ when the flow reaches its final steady state. In Figure 11, a pair of stationary recirculating eddies develops behind the cylinder. The length of recirculating region, L, from the rearmost point of the cylinder to the end of the wake, the separation angle agree θ_s, and the drag coefficient C_D is compared with previous computational and experimental data, are listed in Table IV. It was found that both the geometrical and dynamical parameters agree well with the results of previous studies.

Figure 12 shows time-dependent behaviour of streamline contours for $Re = 100$. From Figure 12, it is found that the most attractive feature of the vortex shedding behind a circular cylinder, the periodic variation of the flow field has been successfully reproduced in this study. The two characteristic parameters, the drag and lift coefficients, are defined as below,

$$C_D = \frac{\mathbf{F}x}{\rho U^2 a}, \quad C_L = \frac{\mathbf{F}y}{\rho U^2 a} \tag{72}$$

where **F** is the total force acting on the circular cylinder, which arises from the surface pressure and shear stress. Figure 13 shows the final periodic state of these two parameters. It is found

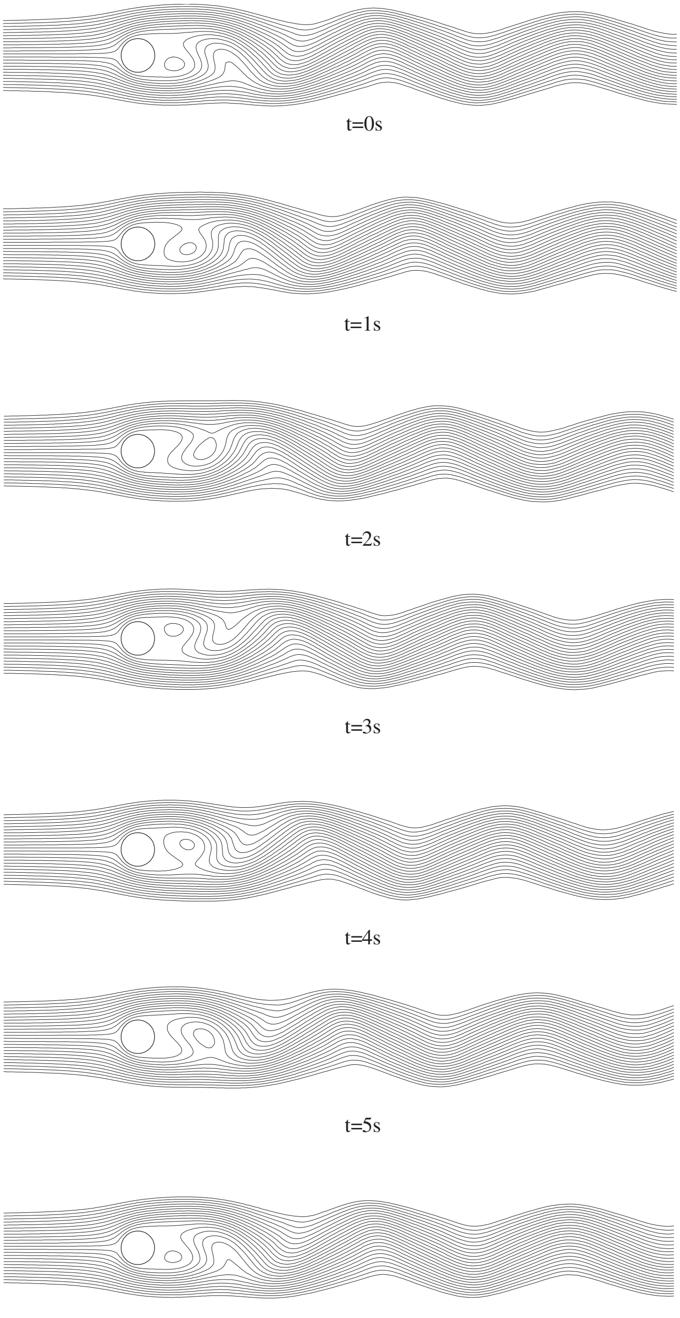

t=0s

t=1s

t=2s

t=3s

t=4s

t=5s

t=6s

Figure 12. Time-evolution of streamlines for $Re = 100$ (Type II).

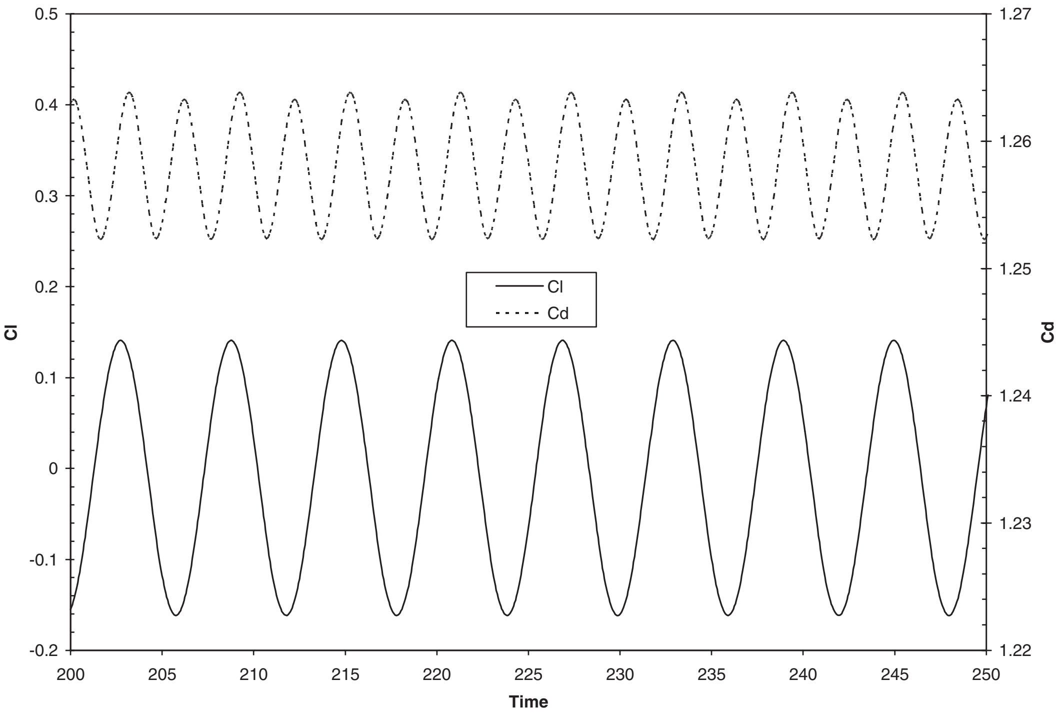

Figure 13. The time-evolution of lift and drag coefficients for $Re = 100$ (type I).

Table V. Comparison of the average drag coefficient $\bar{C}_D$, and Strouhal (St) number.

	$\bar{C}_D$	St
Reference [34]	1.25	—
Reference [35]	1.28	—
Reference [36]	1.28	0.16
Reference [37]	1.287	0.161
Present (Type I)	1.257	0.167
Present (Type II)	1.273	0.167

that the lift coefficient oscillates more strongly than the drag coefficient. The drag coefficient varies nearly twice as fast as the lift coefficient. This is because of the drag coefficient is affected by vortex shedding processes from both sides of the cylinder.

The average drag coefficient and Strouhal number ($St = fD/U$, where f is the shedding frequency) are calculated and listed in Table V. The vortex shedding frequency is obtained by measuring the final period of the lift coefficient. The results from previous experimental measurements and numerical simulations are also included for comparison. Good agreement is observed between these results.

5. CONCLUSIONS

The meshfree weak–strong (MWS) form method is successfully formulated and applied to simulate both steady and unsteady problems of incompressible flow. The numerical examples confirm the following important advantages of the present method:

(1) The present method requires no mesh and works very well with arbitrary nodal distribution.
(2) The computational cost of numerical integration on field nodes, which is the bottleneck problem for other meshfree methods based on the weak form formulation (especially when they are applied to the non-linear problems), is reduced greatly by only evaluating the integration on the nodes on the natural boundary.
(3) The difficulty of imposing the Neumann boundary condition for the other meshfree collocation methods is conveniently removed by using local weak form equation on the nodes there.
(4) The present MWS method has good efficiency as well as high accuracy.

REFERENCES

1. Liu GR. *Mesh Free Methods*: *Moving Beyond the Finite Element Method*. CRC Press: Boca Raton, FL, 2002.
2. Gingold RA, Monaghan JJ. Smoothed particle hydrodynamics: theory and application to non-spherical stars. *Monthly Notices of the Royal Astronomical Society* 1977; **181**:375–389.
3. Liszka T, Orkisz J. The finite difference methods at arbitrary irregular grids and its applications in applied mechanics. *Computers & Structures* 1980; **11**:83–95.
4. Oñate E, Idelsohn S, Zienkiewicz OC, Taylor RL, Sacco C. A stabilized finite point method for analysis of fluid mechanics problems. *Computer Methods in Applied Mechanics and Engineering* 1996; **139**:315–346.
5. Belytschko T, Lu YY, Gu L. Element-free Galerkin methods. *International Journal for Numerical Methods in Engineering* 1994; **37**:229–256.
6. Atluri SN, Zhu T. A new meshless local Petrov–Galerkin (MLPG) approach in computational mechanics. *Computational Mechanics* 1998; **22**:117–127.
7. Atluri SN, Kim HG, Cho JY. A critical assessment of the truly meshless local Petrov–Galerkin (MLPG), and local boundary integral equation (LBIE) methods. *Computational Mechanics* 1999; **24**:348–372.
8. Gu YT, Liu GR. A meshless local Petrov–Galerkin method for free and forced vibration analyses for solids. *Computational Mechanics* 2001; **27**(3):188–198.
9. Gu YT, Liu GR. A meshless local Petrov–Galerkin (MLPG) formulation for static and free vibration analysis of thin plates. *CMES—Computer Modeling in Engineering & Sciences* 2001; **2**(4):463–476.
10. Liu GR, Gu YT. A local radial point interpolation method (LRPIM) for free vibration analyses of 2-D solids. *Journal of Sound and Vibration* 2001; **246**(1):29–46.
11. Gu YT, Liu GR. A local point interpolation method for static and dynamic analysis of thin beams. *Computer Methods in Applied Mechanics and Engineering* 2001; **190**(42):5515–5528.
12. Mukherjee YX, Mukherjee S. Boundary node method for potential problems. *International Journal for Numerical Methods in Engineering* 1997; **40**:797–815.
13. Gu YT, Liu GR. A boundary point interpolation method for stress analysis of solids. *Computational Mechanics* 2002; **28**:47–54.
14. Gu YT, Liu GR. A boundary radial point interpolation method (BRPIM) for 2-D structural analyses. *Structural Engineering and Mechanics* 2003; **15**(5):535–550.
15. Liu GR, Gu YT. A truly meshless method based on the strong–weak form. In *Advances in Meshfree and X-FEM Methods*, Liu GR (ed.). World Scientific: Singapore, 2002; 259–261.
16. Liu GR, Gu YT. A meshfree method: meshfree weak–strong (MWS) form method for 2-D solids. *Computational Mechanics* 2003; **33**(1):2–14.
17. Cheng M, Liu GR. Finite point method for analysis of fluid flow. In *Proceedings of the 4th Asia-Pacific Conference on Computational Mechanics*, Wang CM, Lee KH, Ang KK (eds), Singapore, 15–17 December, 1999; 1015–1020.
18. Cheng M, Liu GR. A novel finite point method for flow simulation. *International Journal for Numerical Methods in Fluids* 2002; **39**(12):1161–1178.

19. Xu XG, Liu GR. A local-function approximation method for simulating two-dimensional incompressible flow. In *Proceedings of the 4th Asia-Pacific Conference on Computational Mechanics*, Wang CM, Lee KH, Ang KK (eds), Singapore, 15–17 December, 1999; 1021–1026.
20. Shu C, Ding H, Yeo KS. Local radial basis function-based differential quadrature method and its application to solve two-dimensional incompressible Navier–Stokes equations. *Computer Methods in Applied Mechanics and Engineering* 2003; **192**:941–954.
21. Wu YL, Liu GR. A meshfree formulation of local radial point interpolation method (LRPIM) for incompressible flow simulation. *Computational Mechanics* 2003; **30**(5–6):355–365.
22. Lancaster P, Salkauskas K. *Curve and Surface Fitting*, *An Introduction*. Academic Press: New York, 1986.
23. Wendland H. Piecewise polynomial, positive definite and compactly supported radial basis functions of minimal degree. *Advances in Computational Mathematics* 1995; **4**:389–396.
24. Kansa EJ. Multiquadrics—a scattered data approximation scheme with applications to computational fluid dynamics. *Computers & Mathematics with Applications* 1990; **19**(8/9):127–145.
25. Bogomolny A. Fundamental solution method for elliptic boundary value problems. *SIAM Journal on Numerical Analysis* 1985; **22**:644–669.
26. Atluri SN, Kim HG, Cho JY. A critical assessment of the truly meshless local Petrov–Galerkin (MLPG) and local boundary integral equation (LBIE) methods. *Computational Mechanics* 1999; **24**:348–372.
27. Liu GR, Yan L. A modified meshless local Petrov–Galerkin method for solid mechanics. In *Advances in Computational Engineering and Sciences*, Atluri SN, Brust FW (eds). Tech Science Press: Palmdale, CA, 2000; 1374–1379.
28. de Vahl Davis G. Natural convection of air in a square cavity: a benchmark numerical solution. *International Journal for Numerical Methods in Fluids* 1983; **3**:249–264.
29. Jiang CB, Kawakara M. The analysis of unsteady incompressible flows by a three-step finite element method. *International Journal for Numerical Methods in Fluids* 1993; **16**:793–811.
30. Dennis SCR, Chang GZ. Numerical solutions for steady flow past a circular cylinder at Reynolds number up to 100. *Journal of Fluid Mechanics* 1980; **42**:471.
31. Nieuwstadt F, Keller HB. Viscous flow past circular cylinders. *Computers & Fluids* 1973; **1**:59.
32. Fornberg B. A numerical study of steady viscous flow past a circular cylinder. *Journal of Fluid Mechanics* 1980; **98**:819.
33. He XY, Doolen GD. Lattice Boltzmann method on a curvilinear coordinate system: flow around a circular cylinder. *Journal of Computational Physics* 1997; **134**:306–315.
34. Tritton DJ. Experiments on the flow past a circular cylinder at low Reynolds numbers. *Journal of Fluid Mechanics* 1959; **6**:547–567.
35. Jordan SK, Fromm JE. Oscillatory drag, lift, and torque on a circular cylinder in a uniform flow. *Physics of Fluids* 1972; **15**:371–376.
36. Braza M, Chassaing P, Ha Minh H. Numerical study and physical analysis of the pressure and velocity fields in the near wake of a circular cylinder. *Journal of Fluid Mechanics* 1986; **165**:79.
37. He XY, Doolen GD. Lattice Boltzmann method on a curvilinear coordinate system: vortex shedding behind a circular cylinder. *Physical Review* 1997; **56**:434–440.